WILEY | Hindawi

Research Article

Multiscale Fracturing in Medium- to Low-Rank Coals and Its Implications on Coalbed Methane Production in the Baode Area, Eastern Ordos Basin, China

Wei Zhang (ID)**, Baoshan Zhao** (ID)**, Qingfeng Zhang** (ID)**, Jikun Zhang** (ID)**, Ziling Li** (ID)**,
Xiaoguang Sun (ID)**, and Mingming Yan** (ID)

PetroChina Coalbed Methane Company Limited, Beijing, China 100028

Correspondence should be addressed to Ziling Li; lzl_cbm@petrochina.com.cn

Coal fractures are crucial in affecting the production of methane from coal. Multiscale fracturing and its implications on coalbed methane production have still not been fully understood. Herein, we present a case study, combining underground coal mine surveying and specimen, thin section, and scanning electron microscope observations for illustrating the ~m-, ~cm-, ~mm-, and ~μm-scale fractures present in the Baode area, eastern Ordos Basin, China. Then, the fracture connectivity is evaluated by helium permeability and mercury porosimetry measurement. The coals are mainly of semibright, semidull, and dull macrolithotypes. And main maceral composition is vitrinite, accounting for 73%~95%, with around 26% inertinite. The coals are ultralow-ash and low-ash content, belonging to high-volatile bituminous coal. The ~m scale fractures can penetrate the whole coal seams, dominant by S-N and following E-W direction, which were generated during the Yanshanian and Himalayan movements. The ~cm fractures are generally parallel to the lamina, influenced by the bright and dull coal band extension caused by the depositional differences. The ~mm fractures are mainly shown as endogenous fractures perpendicular to the lamina restricted within bright macrolithotypes. There are also ~mm fractures that are perpendicular to the lamina while penetrating dull components and fractures parallel to the lamina. The ~μm fractures are widely distributed and connect each other. Some of the fractures are filled with carbonate and clay minerals and are beneficial for methane migration, caused by hydraulic fracturing. The average mercury withdrawal efficiency of the coals was 75%. The helium permeability of the coals was between 10×10^{-3} and 50×10^{-3} μm^2, indicating good fracture connectivity. The study findings, which indicated the presence of fractures of different scales in the coals studied, can be used for fully understanding the coalbed methane performance of medium- and low-rank coals.

1. Introduction

The total coalbed methane (CBM) resources in China that are within 2000 m from the ground are estimated to be 36.81 trillion cubic meters of which medium- and low-rank coals accounted for 7.8 and 14.7 trillion cubic meters, respectively [1, 2]. The CBM production in China is currently dominated by medium (maximum vitrinite reflectance, $R_{o,max}$, = 0.7% – 2.0%)-to-high ($R_{o,max}$ > 2.0%) rank coals; most of the production wells are located in the southern Qinshui Basin and eastern Ordos Basin [3, 4]. Low-rank CBM has not yet been widely developed in China despite its huge production potential. The coals used from the Powder River Basin in the United States and Surat Basin in Australia for commercial production of CBM are typically low-rank coals [5–7]. The Baode area is the most successful middle-to-low rank–CBM production area in China. The coal reservoir characteristics have not been widely explored thus far.

Coal permeability is critical in influencing CBM migration and production, which are both affected by coal matrix pores and fractures [8–10]. Even though hydraulic fracturing is typically used during CBM production, the initial permeability of coal is still a dominant controlling factor of CBM well performance [11, 12]. The permeability of coal

is mainly influenced by its fractures, including intrageneric cleats and exogenous joints. The fracture size and connectivity are the main factors affecting the permeability of coal reservoirs [13, 14]. Extensive studies using methods, such as gas adsorption and desorption experiments with N_2, CO_2, or Ar, as the medium; three-dimensional imaging, such as micro- and nano-X-ray computed-tomography, focused ion beam scanning electron microscopy, and helium ion microscopy; and fluid intrusion techniques, such as mercury intrusion porosimetry and nuclear magnetic resonance, have been conducted for exploring micropore occurrence in coal [15–20]. However, as for the traditional and direct observation of the fracture developed in the coals, it is still lacking clear recognition [21]. The calculation of the number of fractures is difficult because of the complexity and heterogeneity of the fractures. Mechanical parameters are used to estimate coal fracture, fracture occurrence, and fracture numbers [22–24]. Coal fractures have to be studied using coal core and coal mining surface observations and geophysical methods.

The Baode area, one of the most successful CBM production areas in China, was selected as the study area. A series of comprehensive studies were conducted for investigating fracture occurrence in coal, followed by a discussion on its influence on CBM production. The key purpose of the study was to identify the fracture extension in low-to-middle rank coals, which could help understand methane migration and production. The results would help understand low rank–CBM production in other basins where coals with similar properties are present.

2. Geological Setting

The Baode area in Shanxi is on the eastern margin of the Ordos Basin, and its tectonic location is along the northern segment of the Jinxi fold [25]. The area, which has a stable structure, is located in the transitional area between the basin margin and the inner basin (Figure 1). Large faults and folds are less developed, with most small fault strikes along the near north-south direction. The coal exhibits a monoclinic structure along the near north-south direction with a westward inclination. The dip angle of the coal seam is small. The coal measure mainly comprises fine gravel sandstone, siltstone, and carbonaceous mudstone. It has small amounts of medium-grained and coarse-grained sandstones. The coal-bearing strata comprise the Upper Carboniferous-to-Permian Benxi, Taiyuan, and Shanxi Formations. Ordovician limestone is below the coal measure, whereas Triassic fluvial deposits are above it.

3. Materials and Methods

3.1. Coal Seams and Specimen Observation. Exogenous fractures in the coal seams of the Baode Coal Mine were observed via underground observations. The anatomical points were mainly concentrated on the coal wall of the excavation roadway. The 240 m wide 308 working face of the Baode Coal Mine was continuously tracked and observed while focusing on the development of small structures and microstructures, such as exogenous joints and small faults. The roadway excavation was straight, and small folds were not apparent. The occurrence of exogenous fractures was observed, and their density was estimated. The location and partial filling characteristics of the exogenous fractures associated with the coal seam were marked.

All of the samples were collected from the No. 8 coal seam of the study area. The hand specimen samples could be described using features, such as sample color, structure, composition, macroscopic coal type, luster, fracture, hardness, firmness coefficient, endogenous fracture development characteristics, exogenous fracture development characteristics, and filling characteristics. Coal macrolithotypes can be classified as dull, semidull, semibright, and bright coal. Furthermore, the ~μm scale fracture was detected by a scanning electronic microscope (SEM) [4].

3.2. Proximate, Maceral Composition, and Vitrinite Reflectance Analyses. Proximate analysis, including moisture, ash yield, volatile matter, and fixed carbon content analysis, was performed on 12 samples based on GB/T 212-2001 [26]. Maceral composition analysis was conducted according to ISO 7404–3 : 2009, and the total maceral composition was measured by counting all the macerals present using volume percentages [27, 28]. The R_o values were analyzed using a Leitz MPV3-SP microscope in accordance with the international standard ISO17246: 2010 and China Petroleum Industry Standard SY/T 5124-2012. At least 50 readings from each sample were recorded [29].

3.3. Helium Permeability. Coal permeability was tested using coal columns of 25 mm diameter. It was determined using Darcy's formula, which says that the flow rate of a fluid passing through a rock sample will be directly proportional to the cross-sectional area A of the core and pressure difference ΔP between core inlet and outlet and inversely proportional to the length L of the rock sample, and viscosity μ of the fluid as given in

$$K_g = \frac{2Qp_o\mu L}{A\left(p_{in}^2 - p_{out}^2\right)} \times 1000, \tag{1}$$

where K_g is the gas permeability, 10^{-3} μm^2; A is the cross-sectional area of the core, cm^2; L is the length of the tested core, cm; μ is fluid viscosity, mPa·s; Q is the flow rate at the core outlet under atmospheric pressure, cm^3/s; P_0 is the atmospheric pressure, 0.1 MPa; P_{in} is the pressure at the core inlet, MPa; and P_{out} is the pressure at the core outlet, MPa. The helium viscosity was found to be 0.017 mPa·s when tested.

3.4. Mercury Intrusion Porosimetry. Mercury intrusion porosimetry analysis was performed only on six selected samples because other samples had either quality- or quantity-related issues. The experiment was conducted using a Micromeritics 9310 porosimeter. It was based on the Chinese Oil and Gas Industry Standard SY/T 5346-1994. Before performing the analysis, all samples were dried at 75°C for 48 h. The average pore radius, mercury saturation, and mercury
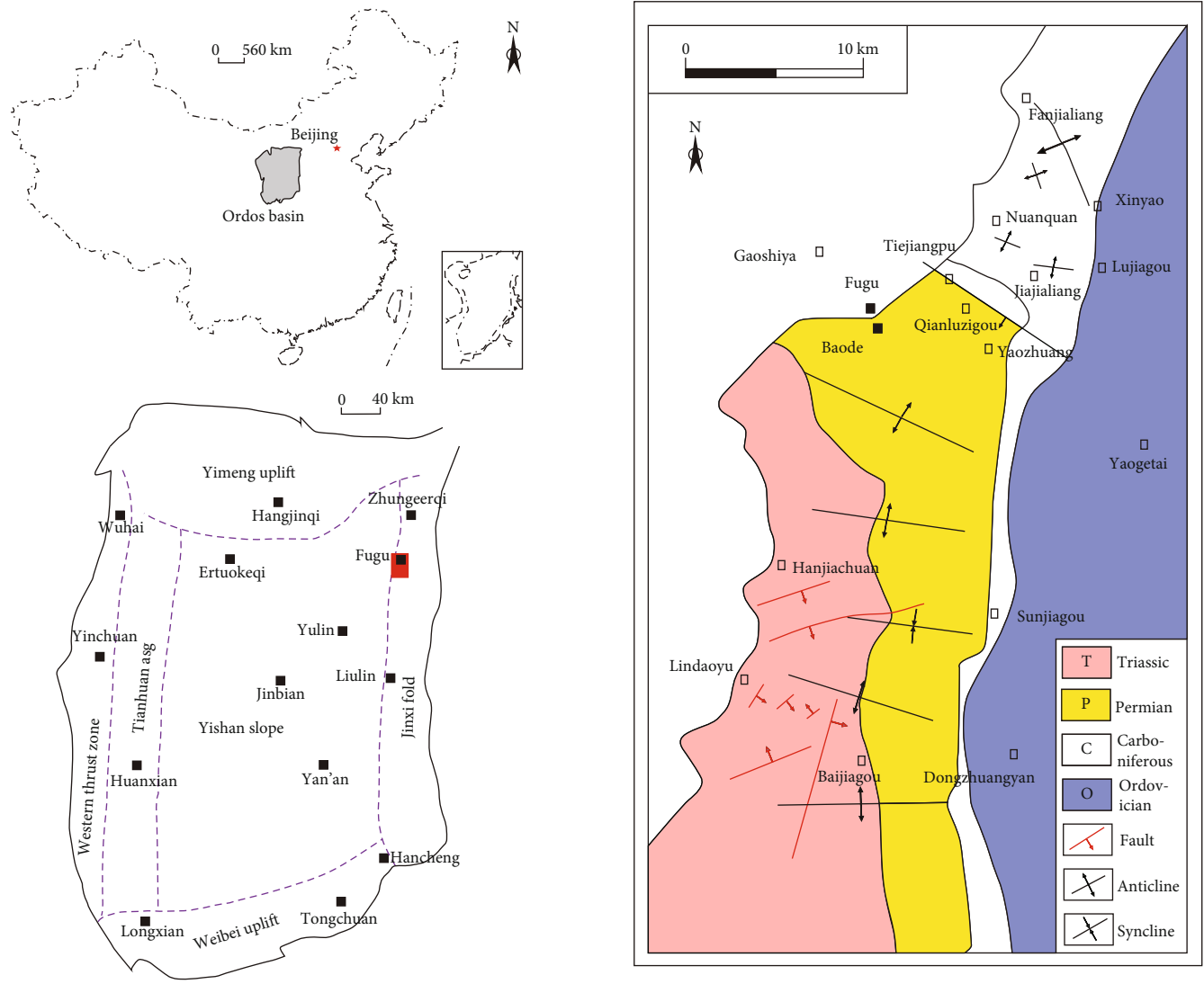
FIGURE 1: Geological setting of the study area.

withdrawal efficiency of the coal in the samples were all recorded [8, 30].

4. Results

4.1. Maceral Composition.
Coal has a high vitrinite content of approximately 73%–95% (Table 1). Its inertinite content is low (<26%). The gelovitrinite content in vitrinite is high, mainly comprising homogeneous vitrinite and collodetrinite. Furthermore, a few samples contained telovitrinite. Vitrodetrinite was present in the samples, and small amounts of collodetrinite and telinite were observed (Figure 2(a)). The inertinite group was dominated by semifusinite and inertodetrinite. Well-preserved fusinite was rarely detected. The interlayers of collodetrinite and homogeneous vitrinite strips and corpogelinite could be observed, as shown in Figure 2(b). Collotelinite is commonly developed with internal pores, and pore deformation occurred during the coalification process (Figures 2(c) and 2(d)).

TABLE 1: Maceral composition of coal in the Baode area in the eastern Ordos Basin of China.

Sample No.	T (%)	G (%)	VD (%)	V (%)	Sf (%)	ID (%)	I (%)	E (%)
BD1	0.13	0.4	0.11	0.64	0.15	0.16	0.31	0.05
BD2	0.52	0.42	0.01	0.95	0.02	0.03	0.05	0.01
BD4	0.17	0.57	0.03	0.77	0.19	0.04	0.23	0
BD7	0.26	0.42	0.05	0.73	0.19	0.07	0.26	0.01
BD8	0.41	0.53	0.01	0.95	0.03	0.01	0.04	0
BD9	0.38	0.33	0.04	0.76	0.14	0.1	0.24	0
BD10	0.34	0.58	0.02	0.94	0.04	0.02	0.06	0.01
BD11	0.29	0.5	0.07	0.86	0.07	0.06	0.13	0
BD12	0.64	0.24	0.03	0.90	0.06	0.03	0.09	0.01
BD14	0.24	0.31	0.16	0.71	0.10	0.16	0.26	0.03

T: telovitrinite; G: gelovitrinite; VD: vitrodetrinite; V: vitrinite; Sf: semifusinite; ID: inertodetrinite; I: inertinite; E: exinite.
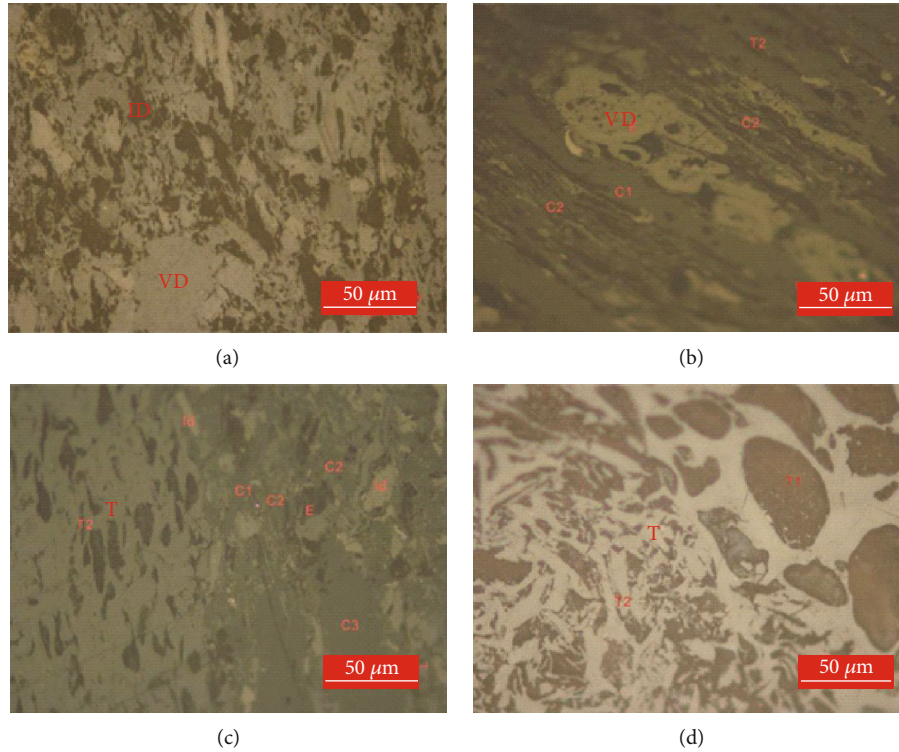
(a)

(b)

(c)

(d)

FIGURE 2: Photomicrographs of macerals present in the samples (T: telovitrinite; VD: vitrodetrinite; ID: inertodetrinite).

TABLE 2: Proximate analysis results and vitrinite reflectances of the samples.

Sample No.	M_{ad} (%)	A_{ad} (%)	V_{ad} (%)	V_{daf} (%)	FC_{ad} (%)	$R_{o,max}$ (%)
BD1	2.16	12.65	23.89	28.04	61.30	1.21
BD2	3.63	9.13	35.09	40.22	52.15	0.85
BD4	3.45	7.72	32.40	36.47	56.43	0.80
BD6	3.19	5.78	36.61	40.22	54.41	0.57
BD7	2.60	16.59	30.88	38.21	49.93	0.99
BD8	3.47	5.12	37.30	40.80	54.12	0.83
BD9	2.65	14.56	32.85	39.68	49.94	0.77
BD10	3.20	5.39	35.22	38.53	56.19	0.86
BD11	2.77	7.86	36.40	40.73	52.97	0.59
BD12	2.70	10.05	34.79	39.87	52.46	0.81
BD13	3.08	7.08	35.57	39.60	54.27	0.76
BD14	2.06	29.52	20.93	30.59	47.49	1.40
Average value	2.91	10.95	32.66	37.75	53.47	0.78

M_{ad}: moisture, air dry basis, %; A_{ad}: ash yield content, air dry basis, %; V_{ad}: volatile, air dry basis, %; daf: dry ash free basis; FC_{ad}: fixed carbon, air dry basis, %; $R_{o,max}$: maximum vitrinite reflectance, %.

4.2. Proximate Analysis. The results of the proximate analysis of the samples indicated that they had stable moisture content of 2%–4% (Table 2). Thus, the coal could be classified as low-moisture coal. The ash yield of the coal varied depending on the constituent minerals. The highest and lowest ash yields were 29.52% and 5.1%, respectively. Thus, the coals found in the study area could be generally classified as ultralow-ash and low-ash coals. The volatile-matter content of the coal was between 28% and 41%. Most of the samples had volatile-matter content between 36% and 41%, indicating that the samples comprised high-volatile bituminous coal. Two samples comprised a volatile-matter content of 28.04% and 30.59%, respectively, belonging to medium volatile bituminous coal. The %R_o values of most samples were between 0.7% and 0.9% with an average of 0.78%. Two samples had a %R_o of 1.21% and 1.40%, which indicated an abnormally high thermal maturity. Most samples contained gas coal and fat coal. A few samples comprised long flame coal.
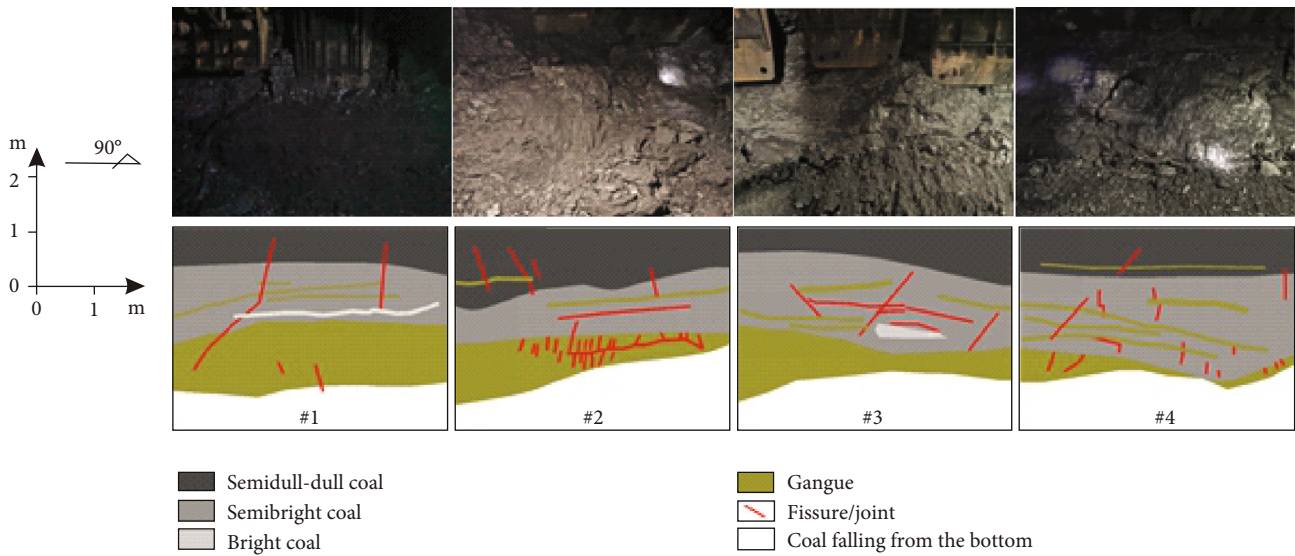
FIGURE 3: Fractures developed in underground coal seams in different locations. The lower figure is a schematic, where white areas represent coal falling out from the bottom, red lines represent exogenous joints, gray-yellow areas represent mudstone gangue, and other colors represent coal stratification of different macroscopic coal types.
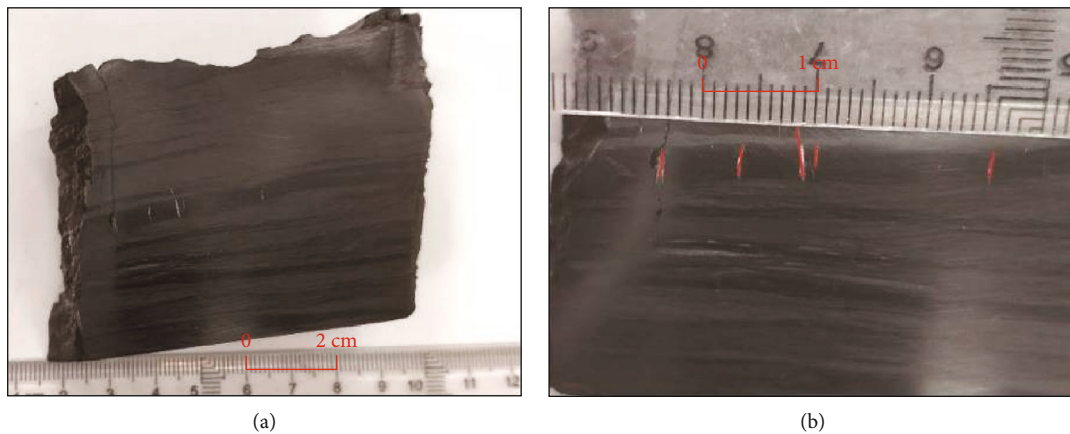

(a)

(b)

FIGURE 4: Fractures (cm-scale) developed in coal cores.

4.3. Occurrence of m-Scale Fractures. The orientation of most of the exogenous fractures in the coal seam of the Baode Coal Mine was along the south-north direction, while the orientation of the other fractures was along the east-west direction. Most of the natural exogenous fractures that had large cross-beds were steeply inclined and tended to dip westward (Figure 3). The linear density of the fractures was 0.7–1.3 strips/10 m, and the distribution of single strips was dominant. Exogenous joints and endogenous fractures were present. Exogenous joints can pass through adjacent macroscopic coal rock-type layers. It is difficult for them to pass through thick gangue layers. The mechanically strong gangue lithology mostly comprises carbonaceous and sandy mudstones. Gangue can develop network joints. Horizontal natural fractures develop in coal reservoirs, mainly in the layers between the coal seam and roof and between the layers within the coal seam.

4.4. Occurrence of cm-Scale Fractures. The samples collected were mainly made of dull coal, semidull coal, and semibright coal, with some bright coal present. The coal in most of the samples had a unified structure or ribbon structure, influenced by peat deposition intervals. The endogenous fractures in the samples were present mainly in bright coal. Yellow-to-white minerals were observed mostly in the endogenous fractures. Four continuous bright coal bands with uneven thicknesses can be observed in Figure 4(a). Their average thicknesses were 4, 3, 1.5, and 0.5 mm. Most of the bright bands had discontinuous fracture distributions. Dull coal bands, with a thickness of approximately 2–6 mm, were present between continuous bright coal bands and discontinuous bright coal bands. Microfractures were well developed in the bright coal bands and were perpendicular to the lamina (Figure 4(b)). They were parallel to each other. At the center of the sample, the fracture density was
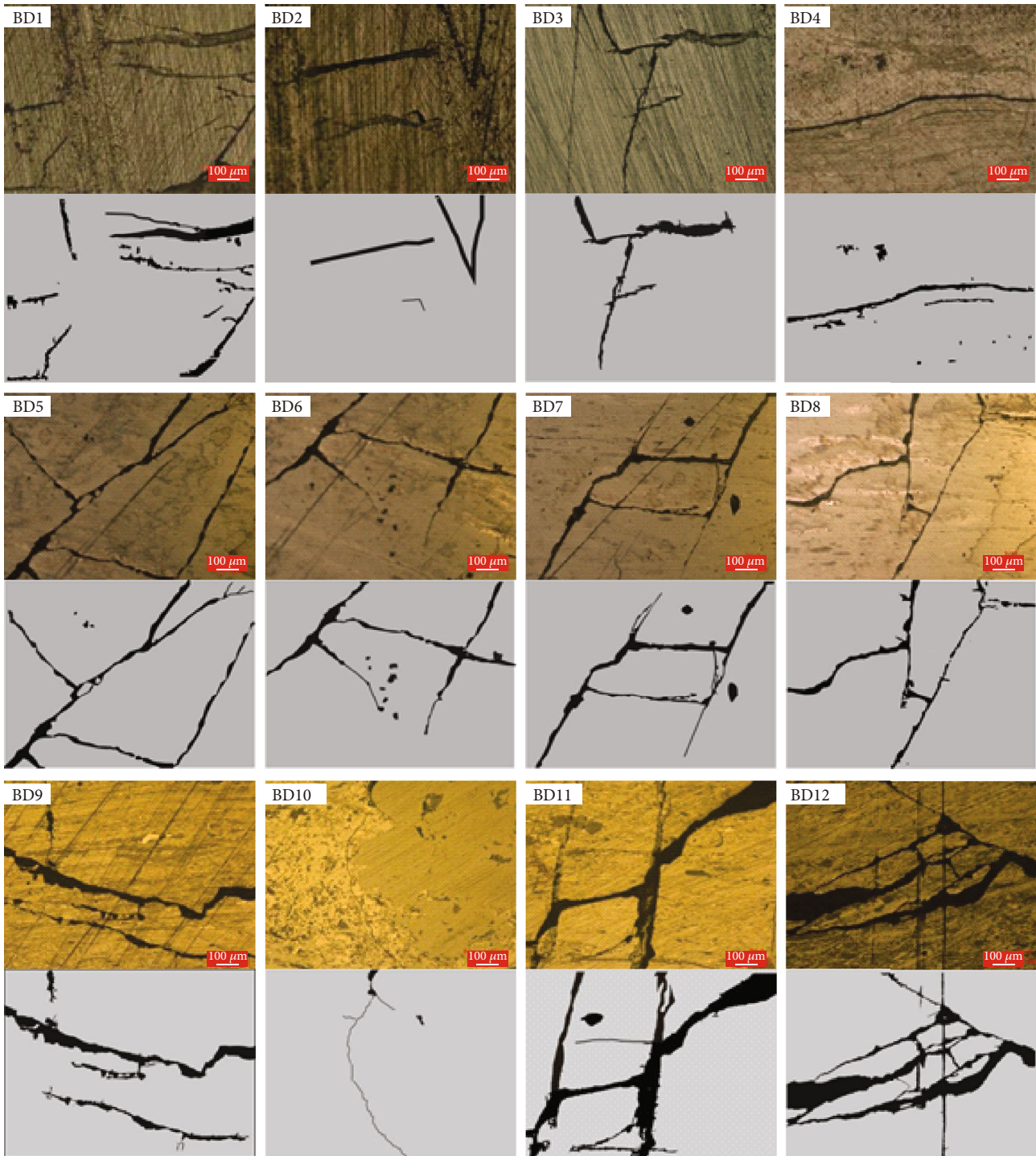
FIGURE 5: Coal fracture distribution in the samples.

approximately 5 over a length of 7 cm. Some fractures were connected to one another. The fractures intersected the bright coal bands at a high angle. However, these fractures generally cannot penetrate the dull bands.

Microcracks were prominent in the continuous bright coal bands. A few microfractures are present in the discontinuous bright coal strips. Microcracks are developed perpendicular to the layers and are parallel to one another.

Yellow-white fillings can be seen in the bright coal strip in the middle. The mineral-filled fissures have a density of 5-7 cm with a spacing of 1.5–11 mm and penetrated the bright coal strip and extended into the dark coal layer. The density of the microcracks that are filled with minerals is 1/cm, and their spacing is between 2 and 5 mm. The dark coal layers have not been penetrated, and there are parallel fractures between the two parallel fractures to connect them.
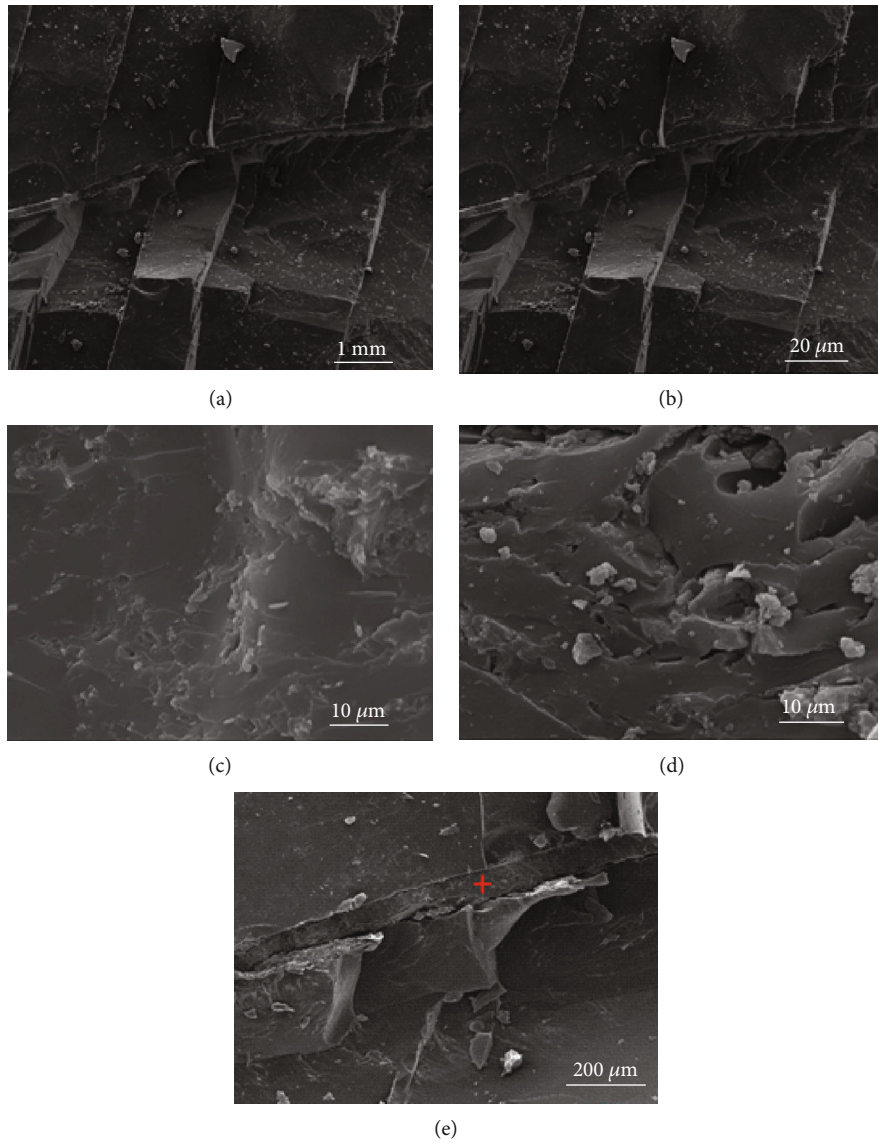
(a)

(b)

(c)
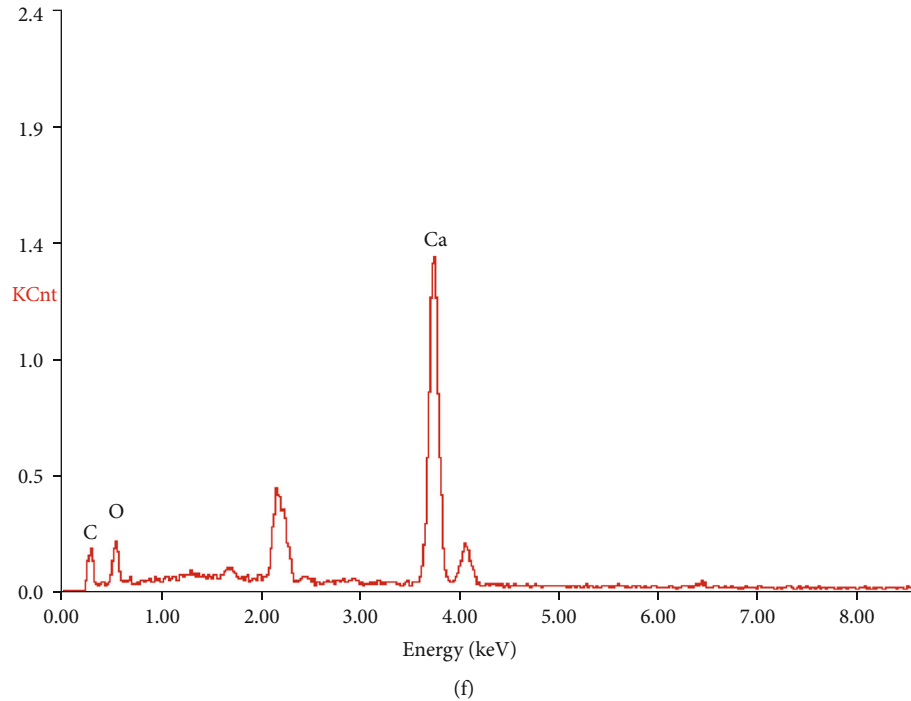

(d)

(e)

Figure 6: Continued.

(f)

FIGURE 6: Fractures and minerals in coal. (a) Endogenous fractures, (b, d) endogenous fissures filled with clay minerals, (c, d) clay minerals, (e) endogenous fractures filled with carbonate minerals, and (f) results of the elemental analysis of the point marked by the red cross in (e).
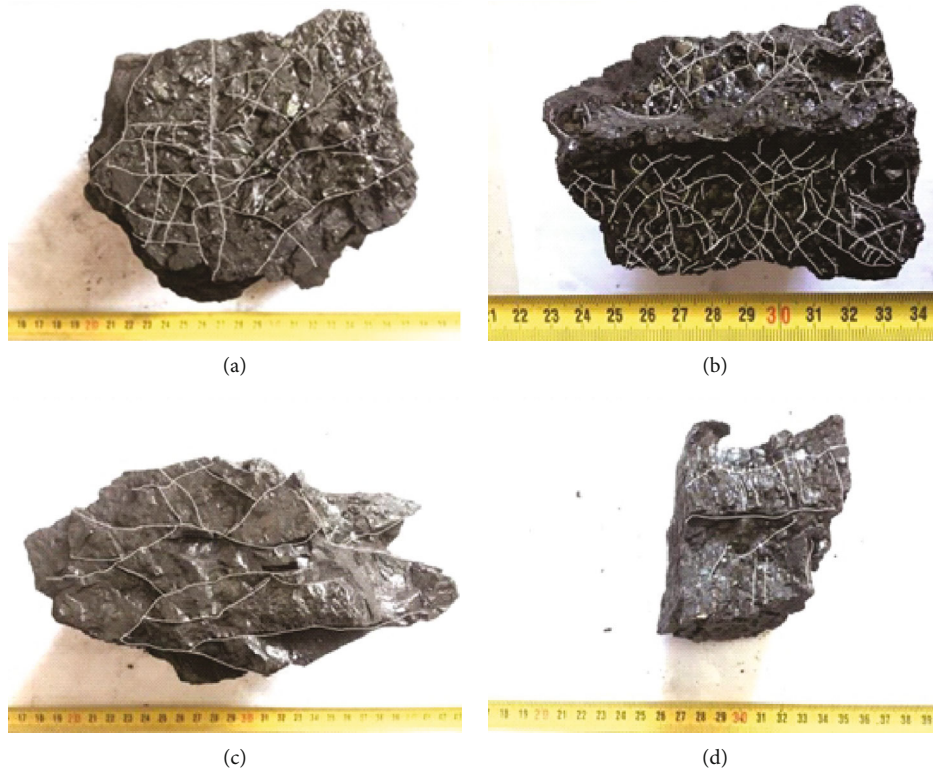

(a)

(b)

(c)

(d)

FIGURE 7: Endogenous fractures and their distribution in coal. (a, b) Interconnected endogenous fractures filled with minerals and (c, d) endogenous fractures without mineral fillings.

Mineral-filled fractures are less developed in the rest of the belts, and the fractures not filled with minerals are similarly developed with a density of approximately 1/cm.

4.5. Occurrence of mm-Scale Fractures. In the thin section, microfractures are widely distributed, penetrating bright and dull coal bands. The fractures are generally unstable

TABLE 3: Mercury porosimetry results of the samples.

Samples	Porosity (%)	Average pore radius (nm)	Mercury saturation (%)	Mercury withdrawal efficiency (%)
BD01	3.82	6.63	37.42	90.12
BD02	6.12	6.73	57	64.58
BD03	5.95	6.53	55.79	71.93
BD08	6.37	9.36	60.22	57.16
BD09	2.8	6.98	34.8	92.15
BD10	4.14	11.18	60.41	71.51

TABLE 4: Helium permeability test results of the samples.

Samples	Fractures	Confining pressure (MPa)	Inlet pressure (MPa)	Outlet pressure MPa)	Flow rate (cm^3/s)	Permeability (10^{-3} μm^2)
1	Developed	7.0	1.5	1.0	3.58	40.78
		9.0	1.5	1.0	3.17	36.04
		11.0	1.5	1.0	2.92	33.19
		13.0	1.5	1.0	2.58	29.40
		15.0	1.5	1.0	2.42	27.50
		17.0	1.5	1.0	2.08	23.71
2	Developed	7.0	2.0	1.0	6.67	31.61
		9.0	2.0	1.0	5.33	25.29
		11.0	2.0	1.0	5.00	23.71
		13.0	2.0	1.0	4.33	20.55
		15.0	2.0	1.0	3.83	18.18
		17.0	2.0	1.0	3.50	16.60
3	Developed	7.0	1.5	1.0	1.00	8.88
		9.0	1.5	1.0	0.92	8.14
		11.0	1.5	1.0	0.72	6.37
		13.0	1.5	1.0	0.58	5.18
		15.0	1.5	1.0	0.33	2.96
		17.0	1.5	1.0	0.29	2.59
4	Developed	7.0	2.0	1.0	2.25	8.33
		9.0	2.0	1.0	2.12	7.83
		11.0	2.0	1.0	1.92	7.09
		13.0	2.0	1.0	1.45	5.37
		15.0	2.0	1.0	1.17	4.32
		17.0	2.0	1.0	1.08	4.01

and are root-shaped, geese-shaped, cone-shaped, and side column-shaped with coarse fracture surfaces. These fractures are not fully filled, and some of the broken coal matrix particles could be seen. The fractures are connected even though most of the fractures are confined to the bright coal band (Figure 5).

The mm-scale fractures can be divided into three categories. The first type of fractures is perpendicular to the lamina and confined to the bright coal bands. A few have small openings and are filled with minerals. They are not connected to other fractures. The second type of fractures, which are either root-shaped or brush-shaped, is perpendicular to the lamina. They extend into bright and dull coal bands. Most of these fractures have large openings filled with

minerals. The minerals and coal components are quite apart from each other, not completely filled. The fractures generated during the geological evolution of coal are connected together, which benefits methane migration and production. The third type of fractures is parallel to the lamina, and they are mainly at the junctions of the bright coal bands and silk charcoal or within silk charcoal itself.

4.6. Occurrence of μm-Scale Fractures. The SEM images indicated that endogenous fractures were widely distributed in the samples tested. Some fractures were parallel to each other, with some being closed while some are open, as shown in Figures 6(a) and 6(b). The fractures indicated that the inner connectivity of the coal in the study area was
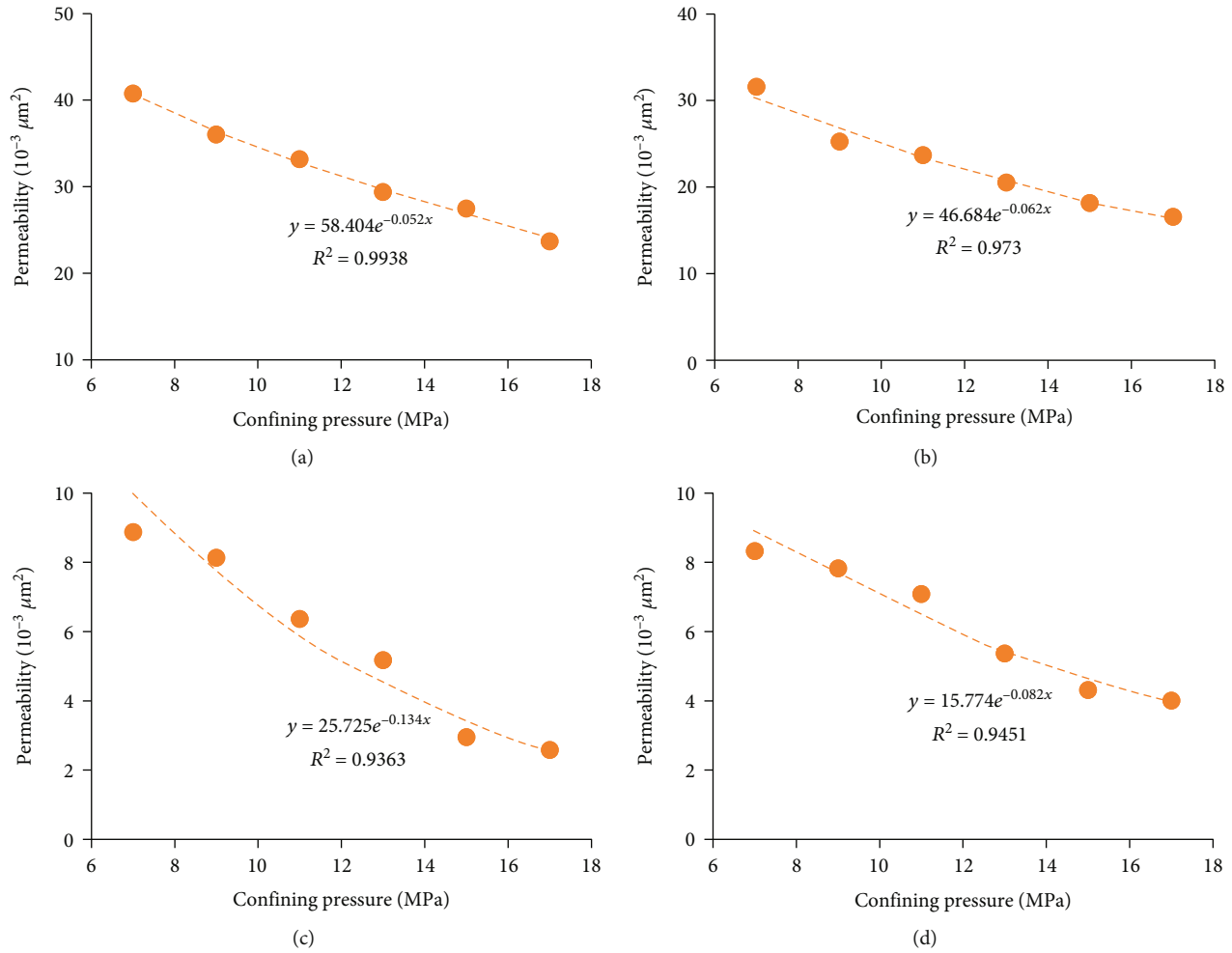
(a)

(b)

(c)

(d)

Figure 8: Permeability influenced by the confining pressure.

satisfactory, which is beneficial for methane migration. Similar to the fractures, the pores, namely, gas pores and residual plant tissue pores, were well developed, as shown in Figures 6(c) and 6(d). The coals had been generating methane as indicated by their thermal maturity (Table 2). The coals, however, were in their early coalification stage with residual pores apparent, which is favorable for methane migration and production.

5. Discussion

5.1. Fracture Connectivity and Its Influences. The formation of endogenous fractures in coal depends on the type of coal. Endogenous fractures often develop in bright coal bands (Figure 7). They are irregularly distributed, and the directions of some fractures were visible. One group of fractures was perpendicular to the lamina, whereas the fractures in the other two groups were parallel to the lamina, and some of the fractures in the first group were connected to the fractures in the other group at a certain angle, as shown in Figures 7(a) and 7(c). The fracture surfaces were flat, and some fractures were filled with minerals. The endogenous fissures on the hand specimens formed an irregular network and were filled with minerals. SEM energy spectrum analysis

revealed that the endogenous fractures were filled mostly with carbonate minerals, followed by clay minerals (Figure 6(f)). The closure of the fractures can decrease coal permeability, and the existence of closed fractures can be beneficial for methane production. The fractures that are not filled with minerals can get easily extended during hydraulic fracturing. Thus, the development of both forms of fractures is advantageous for CBM production [31].

Mercury porosimetry can indicate the presence of fractures and help determine pore connectivity of coal. Table 3 shows that the mercury intrusion porosity of the sample ranges from 2.8% to 6.37% (average porosity = 4.87%). The pore throat diameter of the coal ranges from 6.53 to 16.18 nm, with an average of 7.9 nm. The approximate average mercury saturation is 50.94%, and the approximate average mercury withdrawal efficiency is 74.58%. The samples exhibit high mercury withdrawal efficiency, implying satisfactory pore and fracture connectivity. The amount of mercury injected gradually increases at first; the mercury injection saturation is within 10%. When the pressure reaches 20–50 MPa, the amount of mercury injected increases rapidly until mercury injection saturation is achieved, indicating that the micropores are rich in the sample. The mercury withdrawal curve is roughly similar to the

mercury injection curve. The high mercury withdrawal efficiency indicates that the pores are mostly open and that they have good connectivity—favorable for CBM production [32, 33].

5.2. Influence of Fractures on Coal Permeability. Two series of coal permeability tests were conducted under different confining stresses to determine the influence of the fractures on the permeability of the coal (Table 4). The original permeabilities of the two series of coals with fractures were 40.78 and $31.61 \times 10^{-3} \mu m^2$ while the permeabilities of the coals that did not have fractures were only 8.88×10^{-3} and $8.33 \times 10^{-3} \mu m^2$. Coal permeability was tested under a confining pressure of 7 MPa and at a coal burial depth of 700–800 m. Coal permeability was influenced by the confining pressure and decreased exponentially as the pressure was increased from 7 to 17 MPa (Figure 8). As the burial depth increased, the fractures started to influence coal permeability. Coals with a high initial permeability can improve the channel flow in the coal mine. The permeabilities of the two coals with fractures were 23.71 and $16.60 \times 10^{-3} \mu m^2$ at 17 MPa while the permeabilities of the two coals without fractures were only 2.59 and $4.01 \times 10^{-3} \mu m^2$ at 17 MPa. Compared with the permeability of the coals at other CBM production blocks, such as the Shizhuang Block, the permeability of the coals in the study area was high, which benefits CBM production [31].

6. Conclusions

Coal macrolithotypes contain mostly semibright, semidull, and dull coals. The main maceral group found in coal is vitrinite (73%–95%). The inertinite content in coal is approximately 26%. Collodetrinite and corpogelinite are the dominant subgroups of vitrinite, whereas semifusinite and inertodetrinite are the dominant subgroups of inertinite. High-volatile bituminous coal has ultralow-ash or low-ash content.

The m-scale fractures in coal seams are mostly in the south-north direction. Some fractures are in the east-west direction. The fractures can penetrate entire coal seams while was blocked the coal gauge. These fractures have been generated during the Yanshanian and Himalayan movements.

The cm-scale fractures are parallel to the lamina and are influenced by the bright and dull coal bands. The mm-scale fractures are of three types. Most of them are endogenous fractures perpendicular to the lamina and are confined to the bright coal bands. The other two types are the fractures perpendicular to the lamina, penetrating the dull coal bands and the fractures parallel to the lamina. The μm-scale fractures are widely distributed and connect coal matrix pores.

Some fractures are filled with carbonate and clay minerals and are arranged as connected networks, which are beneficial for methane production after fracturing. Mercury porosimetry measurements and helium tests show that the coal in the study area has high permeability in the wide range of $10 \times 10^{-3} – 50 \times 10^{-3} \mu m^2$. Coal permeability is exponentially related to the confining stress and is influenced by the fracture closure under high confining pressures.

Data Availability

The data has been included in the ms.

Conflicts of Interest

The authors declare that they have no conflicts of interest.

Acknowledgments

References

[1] R. M. Flores, *Coal and Coalbed Gas: Fueling the Future*, Elsevier Science Publishing Co Inc, United States, 2014.

[2] Y. Qin, T. A. Moore, J. Shen, Z. Yang, Y. Shen, and G. Wang, "Resources and geology of coalbed methane in China: a review," *International Geology Review*, vol. 60, pp. 1–36, 2017.

[3] Y. Li, J. Yang, Z. Pan, S. Meng, K. Wang, and X. Niu, "Unconventional natural gas accumulations in stacked deposits: a discussion of Upper Paleozoic coal-bearing strata in the east margin of the Ordos Basin, China," *Acta Geologica Sinica-English Edition*, vol. 93, no. 1, pp. 111–129, 2019.

[4] Y. Li, Z. Wang, Z. Pan, X. Niu, Y. Yu, and S. Meng, "Pore structure and its fractal dimensions of transitional shale: a cross-section from east margin of the Ordos Basin, China," *Fuel*, vol. 241, pp. 417–431, 2019.

[5] B. Walter, "Coalbed gas systems, resources, and production and a review of contrasting cases from the San Juan and Powder River basins," *AAPG Bulletin*, vol. 86, no. 11, pp. 1853–1890, 2002.

[6] C. A. Rice, R. M. Flores, G. D. Stricker, and M. S. Ellis, "Chemical and stable isotopic evidence for water/rock interaction and biogenic origin of coalbed methane, Fort Union Formation, Powder River Basin, Wyoming and Montana U.S.A.," *International Geology Review*, vol. 76, no. 1-2, pp. 76–85, 2008.

[7] L. H. Hamilton, J. S. Estrela, and S. D. Golding, "Geological interpretation of gas content trends, Walloon Subgroup, eastern Surat Basin, Queensland, Australia," *International Journal of Coal Geology*, vol. 101, pp. 21–35, 2012.

[8] T. A. Moore, "Coalbed methane: a review," *International Journal of Coal Geology*, vol. 101, pp. 36–81, 2012.

[9] Y. Li, J. Yang, Z. Pan, and W. Tong, "Nanoscale pore structure and mechanical property analysis of coal: an insight combining AFM and SEM images," *Fuel*, vol. 260, p. 116352, 2020.

[10] S. Karimpouli, P. Tahmesbi, and H. L. Ramandi, "A review of experimental and numerical modeling of digital coalbed methane: imaging, segmentation, fracture modeling and permeability prediction," *International Journal of Coal Geology*, vol. 228, article 103552, 2020.

[11] C. Clarkson, N. Solano, R. Bustin et al., "Pore structure characterization of north American shale gas reservoirs using

USANS/SANS, gas adsorption, and mercury intrusion," *Fuel*, vol. 103, pp. 606–616, 2013.

[12] Y. Li, C. Zhang, D. Tang, Q. Gan, X. Niu, and R. Shen, "Coal pore size distributions controlled by the coalification process: an experimental study of coals from the Junggar, Ordos and Qinshui basins in China," *Fuel*, vol. 206, pp. 352–363, 2017.

[13] W. Xu, J. Li, X. Wu, D. Liu, and Z. Wang, "Desorption hysteresis of coalbed methane and its controlling factors: a brief review," *Front Earth Sci-Prc.*, vol. 15, no. 2, pp. 224–236, 2021.

[14] H. Hou, G. Liang, L. Shao, Y. Tang, and G. Mu, "Coalbed methane enrichment model of low-rank coals in multi-coals superimposed regions: a case study in the middle section of southern Junggar Basin," *Front Earth Sci-Prc.*, vol. 15, no. 2, pp. 256–271, 2021.

[15] Y. Ma, M. Wang, R. Ma, and J. Li, "Micropore characteristics and gas-bearing characteristics of marine- continental transitional shale reservoirs in the east margin of Ordos Basin," *Adsorption Science and Technology*, vol. 8, pp. 1–15, 2021.

[16] C. Chen, D. Hu, D. Westacott, and D. Loveless, "Nanometer-scale characterization of microscopic pores in shale kerogen by image analysis and pore-scale modeling," *Geochemistry, Geophysics, Geosystems*, vol. 14, no. 10, pp. 4066–4075, 2013.

[17] M. Blunt, B. Bijeljic, H. Dong et al., "Pore-scale imaging and modelling," *Advances in Water Resources*, vol. 51, pp. 197–216, 2013.

[18] S. Kelly, H. El-Sobky, C. Torres-Verdín, and M. Balhoff, "Assessing the utility of FIB-SEM images for shale digital rock physics," *Advances in Water Resources*, vol. 95, pp. 302–316, 2016.

[19] T. Wu, X. Li, J. Zhao, and D. Zhang, "Multiscale pore structure and its effect on gas transport in organic-rich shale," *Water Resources*, vol. 53, no. 7, pp. 5438–5450, 2017.

[20] S. Zhao, Y. Li, Y. Wang, Z. Ma, and X. Huang, "Quantitative study on coal and shale pore structure and surface roughness based on atomic force microscopy and image processing," *Fuel*, vol. 244, pp. 78–90, 2019.

[21] K. Jiao, S. Yao, W. Hu, and K. Zhang, "The evolution of nanopores and surface roughness in naturally matured coals in South China: an atomic force microscopy and image processing study," *Fuel*, vol. 234, pp. 1123–1131, 2018.

[22] Y. Wang, D. Liu, Y. Cai, Y. Yao, and Z. Pan, "Constraining coalbed methane reservoir petrophysical and mechanical properties through a new coal structure index in the southern Qinshui Basin, northern China: implications for hydraulic fracturing," *AAPG*, vol. 2020, p. 104, 2020.

[23] Y. Cai, D. Liu, J. P. Mathews et al., "Permeability evolution in fractured coal – combining triaxial confinement with X-ray computed tomography, acoustic emission and ultrasonic techniques," *International Journal of Coal Geology*, vol. 122, pp. 91–104, 2014.

[24] S. E. Laubach, R. A. Marrett, J. E. Olson, and A. R. Scott, "Characteristics and origins of coal cleat: a review," *International Journal of Coal Geology*, vol. 35, no. 1-4, pp. 175–207, 1998.

[25] Y. Li, D. Tang, D. Elsworth, and H. Xu, "Characterization of coalbed methane reservoirs at multiple length scales: a cross-section from southeastern Ordos Basin, China," *Energy Fuel.*, vol. 28, no. 9, pp. 5587–5595, 2014.

[26] C. Guo, Y. Xia, D. Ma et al., "Geological conditions of coalbed methane accumulation in the Hancheng area, southeastern Ordos Basin, China: implications for coalbed methane high-yield potential," *Energy Exploration & Exploitation*, vol. 37, no. 3, article 014459871983811, pp. 922–944, 2019.

[27] G. H. Taylor, M. Teichmuller, A. Davis, C. F. K. Diessel, R. Littke, and P. Robert, *Organic Petrology*, Gebruder Borntraeger, Berlin, Germany, 1998.

[28] International Committee for Coal and Organic Petrology (ICCP), "The new vitrinite classification (ICCP System 1994)," *Fuel*, vol. 77, pp. 349–358, 1998.

[29] W. Zhao, X. Li, T. Wang, and X. Fu, "Pore size distribution of high volatile bituminous coal of the southern Junggar Basin: a full-scale characterization applying multiple methods," *Frontiers in Earth Science*, vol. 15, no. 2, pp. 237–255, 2021.

[30] M. Zou, C. Wei, M. Zhang, J. Shen, Y. Chen, and Y. Qi, "Classifying coal pores and estimating reservoir parameters by nuclear magnetic resonance and mercury intrusion porosimetry," *Energy & Fuels*, vol. 27, no. 7, pp. 3699–3708, 2013.

[31] W. Han, Y. Wang, and Y. Li, "Recognizing fracture distribution within the coalbed methane reservoir and its implication for hydraulic fracturing: a method combining field observation, well logging, and micro-seismic detection," *Journal of Natural Gas Science and Engineering*, vol. 92, article 103986, 2021.

[32] Y. Yao and D. Liu, "Comparison of low-field NMR and mercury intrusion porosimetry in characterizing pore size distributions of coals," *Fuel*, vol. 95, pp. 152–158, 2012.

[33] C. R. Clarkson, M. Freeman, L. He et al., "Characterization of tight gas reservoir pore structure using USANS/SANS and gas adsorption analysis," *Fuel*, vol. 95, no. 1, pp. 371–385, 2012.